Journal of the European Ceramic Society **18** (1998) 1089–1099

PII: S0955-2219(98)00013-2
0955-2219/98/$19.00 + 0.00

Microstructure and Mechanical Properties of Slip Cast Sol–Gel Derived Mullite Ceramics

E. Tkalcec,* R. Nass, T. Krajewski, R. Rein and H. Schmidt

Institut für Neue Materialien, Im Stadtwald, Gebäude 43, 66123 Saarbrücken, Germany

(Received 28 July 1997; accepted 19 December 1997)

Abstract

Mullite ceramics were processed by pressureless sintering (1620°C, 2 h) of slip cast mullite derived from single-phase gel calcined at 1070°C and attrition milled with ZrO_2 balls. The four-point bending strength was determined from room temperature up to 1400°C. Creep behaviour in compression was determined at stresses of 20 and 100 MPa and temperatures of 1200 to 1450°C. Microstructural and microchemical characterisation of mullite material was performed using scanning (SEM) and high resolving transmission electron microscopy (HRTEM) in conjuction with energy dispersive X-ray spectrometry (EDX). A remarkable abrasion of ZrO_2, and the leaching of magnesium from ZrO_2 grains occurred in milling process. The bending strength and the creep behaviour is determined by residual glassy phase, observed in triple points and at the grain boundaries of mullite/mullite and mullite/ZrO_2 grains. When ZrO_2 grain participates in the formation of triple points, the composition of the glassy phase differs from that at the junction of three mullite grains. The EDX line microanalyses across the mullite/mullite grain boundaries revealed < 5 nm thick SiO_2-rich glassy film. There are some grain boundaries at which only a compositional gradient of SiO_2 occurred. The creep below 1300°C is most likely controlled by grain boundary sliding accommodated by solution–precipitation mechanism, and above by the grain boundary sliding accommodated by viscous flow of SiO_2-rich phase. © *1998 Elsevier Science Limited. All rights reserved*

Keywords: mullite, microstructure, creep, bending strength at high temperature, ZrO_2 abrasion.

*To whom correspondence should be addressed. Fax: +49 681 9300242; e-mail:tkalcec@inm.uni-sb.de

1 Introduction

The sol–gel technique nowadays enables processing of very pure mullite precursors that allow to obtain high density structural mullite materials.[1] Calcination temperature required for removing volatiles and for mullitization amounts to ~1000°C for molecularly mixed and to ~1300°C for diphasic precursors. However, heat treatment activates particle growth and the formation of hard agglomerates. As a result of both—the particle growth and agglomeration—the calcined product generally requires extensive grinding to produce mullite powders that sinter to high relative density. Powders are generally contaminated during milling operations by different impurities, the amount and nature of which depends on milling conditions and media. It is generally considered that zirconia as milling media mostly remains as isolated particle in mullite ceramics.[2] However, the influence of the cations stabilizing the cubic/tetragonal zirconia has to be taken into consideration. These cations are generally silica glass–network modifiers[3] and therefore they may have an effect on the viscosity of glassy phase in sintered mullite. Excellent creep resistance[4] and high mechanical strength at elevated temperatures of mullite without glassy phase are reported in literature.[5,6] However, the existence and particularly the composition of glassy phase at the grain boundaries have a strong influence on mechanical properties at elevated temperatures.[5,7]

The aim of this work is to determine the mechanical properties of slip cast and pressureless sintered mullite derived from sol–gel processed single-phase powder, attrition milled by ZrO_2 balls (Mg-stabilized ZrO_2). Bending strength measurements carried out in the range from ambient temperature to 1400°C, and the compression creep resistance performed from 1200 to 1450°C under stress of 20 and 100 MPa, respectively, are correlated to the microstructure and morphology

investigated by scanning and high-resolving transmission electron microscopy (SEM and HRTEM) and energy dispersive X-ray spectrometry (EDXS). Attention is given to the examination of dissolution of ZrO_2 particles and Mg entering the glassy phase.

2 Experimental Procedure

2.1 Sample preparation

Single phase gel with stoichiometric Al/Si = 3/1 ratio was prepared by using tetraethoxysilane (TEOS) > 98% and aluminum nitrate nonahydrate (ANN) as previously described by Nass *et al.*[8] The gel was dried at 60°C, calcined at 1070°C for 2 h and attrition milled for 8 h in ethanol using ZrO_2 balls as milling media. Slurries with 70 wt% of solid loading were prepared by dispersing the attrition milled powder with addition of 1 wt% of a dispersant in ethanol/water suspension. Plates of $70\times70\times7\,mm^3$ dimensions were prepared by slip casting of slurries. The compacts (green density 62–63% of theoretical density) were heated at the heating rates of $2\,K\,min^{-1}$ up to 1500°C and at the heating rate of $10\,K\,min^{-1}$ up to 1620°C and held at the end temperature for 2 h. The density measurement proved that the ceramics were highly densified (99·2–99·5% of theoretical density). The value of $3.26\,g\,cm^{-3}$ as the average theoretical density of the heat treated powder was used, since the values of between $3{\cdot}25$–$3{\cdot}27\,g\,cm^{-3}$ were obtained by measuring the densities of powders heat-treated under the same condition as slip cast bodies. This value was in good agreement with the calculated density, taking into account that in attrition milled samples 6·77 wt% of ZrO_2 was determined by ICP analysis.

2.2 Characterization techniques

Chemical analysis of calcined and attrition milled powder was performed on gels pre-heated at 1000°C for 2 h, then melted with $Li_2B_4O_7$, dissolved in HNO_3 solution and analysed by ICP-atom emission spectrometer (Jobin Yvon, JY 24). The specific surface area of powders was characterised by nitrogen adsorption/desorption isotherms (B.E.T. method) performed by a surface area instrument (ASAP 2400 V3.00, Micromeritics). The samples were outgassed under vacuum at 120°C. Green density of slip cast compacts was calculated by measuring the dimensions of specimens. Bulk density of sintered compacts was measured by the Archimedes method with distilled water as immersion liquid.

X-ray diffraction analysis (XRD) was carried out on a computer controlled diffractometer using CuK_α radiation (Siemens D500/PSD) with quartz single-crystal monochromator and a curved position sensitive detector. Data were collected in a step scan mode in the interval $5\leq°2\theta\geq70$ with steps of 0·02° and a counting time of 10 s per step. The content of crystalline mullite in calcined and attrition milled samples was determined by quantitative XRD analysis with CaF_2 as an internal standard. Calcined powder (calcination temperature $T = 1070$°C) from which amorphous SiO_2 phase was leached out by 40% HF, was used as mullite standard. The alumina content of the mullite in calcined and milled samples was calculated from the relation of the lattice constant a and the mullite composition.[9] The weight loss up to 1300°C was determined by thermogravimetry (TG).

Micromorphological and microanalytical investigations of sintered compacts were studied on polished and thermally etched surfaces (1500°C, 45′) by SEM equipped with EDXS (JEOL 3 6400 F high resolution SEM and TRACOR X-ray spectrometer). For surface imaging the secondary electron (SE) signals excited at an energy of 10 keV were used, and for X-ray analyses the same energy was applied. For electron microscopic experiments a HRTEM (CM200 FEG, Philips) attached with an energy dispersive X-ray spectrometer (DX-4, EDAX) was used. At a primary energy of 200 keV the morphology and structure of the sintered bodies were studied applying bright field diffraction contrast as well as lattice imaging. Electron transparent regions of the materials were gained by mechanical polishing, dimpling, and Ar+ ion milling as final step. Applying a step scan technique of the electron probe the analyses of elemental distributions along selected lines were carried out. The line of measurement was subdivided into 100 intervals and the intensities of relevant characteristic X-radiations were picked up stepwise by means of EDXS, the time/step amounted to 0·2 s.

Dynamic Young's modulus was determined by ultrasonic measurements (Impulsecho method, $f = 20$ MHz). The hardness and fracture toughness were measured by Vickers indentations with a load of 10 kg. Fracture toughness (K_{IC}) was calculated according to Anstis *et al.*[10] The strength was measured by four-point bending (spans 20 and 40 mm) from RT to 1400°C. The tensile surface was polished using a slurry containing 1 μm diamond grains. The specimens ($3\times4\times45\,mm^3$) were loaded at a constant feeding rate of $0{\cdot}1\,mm\,min^{-1}$. The creep resistance was measured in compression using samples with rectangular cross section ($3\times4\times10\,mm^3$). The measurements were carried out at the constant stresses of 20 and 100 MPa from $T = 1200$°C to $T = 1450$°C, and at $T = 1200$°C and $T = 1400$°C under different stresses from 20 to

100 MPa. The stress exponent (n) and the apparent activation energy (Q) were deduced from the following equation, which expresses the steady state of the creep:

$$\frac{d\varepsilon}{dt} = A \cdot \sigma^n \cdot \exp\left(-\frac{Q}{RT}\right) \quad (1)$$

where $\frac{d\varepsilon}{dt}$ is the steady-state creep rate in s^{-1}, σ the stress in MPa, Q the activation energy for creep process; n (stress exponent) and A are characteristic constants of the material. No stress correction was made for the change in cross-sectional area during the run.

3 Results

The specific surface areas, densities, particle sizes and phase analyses of at 1070°C calcined and attrition milled samples are shown in Table 1. The specific surface area of the specimen increases with attrition milling from 7·7 to 19·2 $m^2 g^{-1}$, whereas the particle size and mullite crystallite size decrease. Greater density of calcined powder (3·20 $g cm^{-3}$), and higher alumina content (determined from the relation a-axis length–alumina content[9]), are characteristic of Al-rich mullite.[11,12] During the milling, the powder becomes partially amorphous, and hydration of the powder takes place as well. Therefore, a somewhat smaller density was obtained for attrition milled specimen than for calcined powder. The content of crystalline mullite in calcined and attrition milled powder was determined by quantitative XRD analysis using CaF_2 as internal standard. The XRD patterns are shown in Fig. 1. In addition to mullite, tetragonal ZrO_2 was determined in the milled specimen. The chemical analysis of as-calcined and after calcination attrition milled powders preheated at 1000°C (Table 2) also show that the milled sample is contaminated with ZrO_2 and MgO. The ratio of MgO/ZrO_2 especially strikes one's eyes because it is much higher than it was expected. According to ICP analysis, Mg-stabilized ZrO_2

Table 1. Specific surface areas, densities, mean particle sizes and phase analyses of powder calcined at 1070°C and attrition milled after calcination

Characteristics	*Powder calcined at 1070°C for 2 h*	
	As-calcined	*Calcined and attrition milled 8 h*
Specific surface area ($m^2 g^{-1}$)	7·7	19·2
Density ($cm^3 g^{-1}$)	3·20	3·08
Particle size d_{50}% (μm)	2·2	0·26
Mullite crystallite size (nm)	76	26
Crystalline phases: (wt%)		
Mullite	97 ± 2[a]	40 ± 2[a]
t-ZrO_2	—	6·77[b]
Al_2O_3 in mullite[c] (wt% and mole%)	75·4/64·4	75·5/64·5
Al/Si molar ratio in mullite	3·62	3·63
Al/Si molar ratio in bulk sample	2·96	2·94
Weight loss from TG	0·3	4·2

[a]Quantitative XRD.
[b]ICP analysis.
[c]Determined from a-axis length.

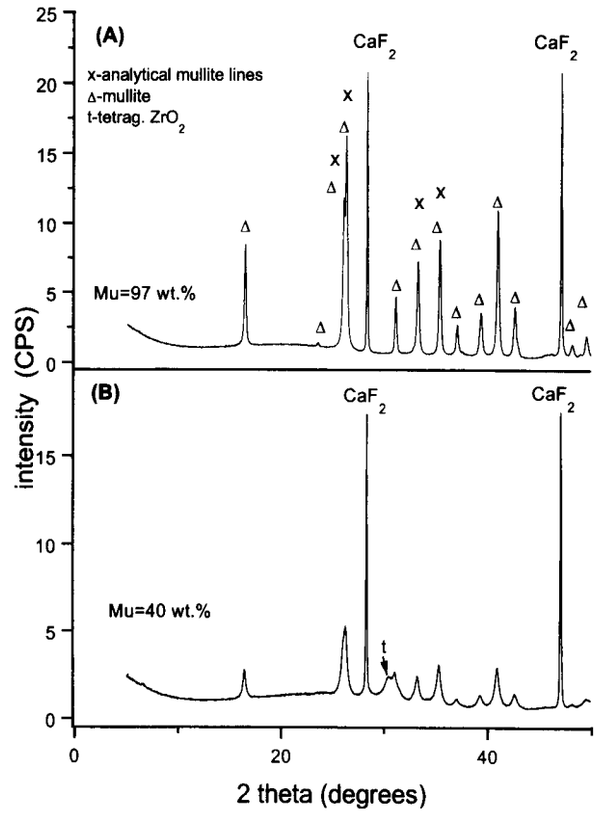

Fig. 1. Quantitative XRD patterns of: (A) calcined and (B) calcined and attrition milled sample. Δ, mullite, x, analytical mullite reflections, CaF_2 was added as internal standard, t, tetragonal zirconia.

Table 2. Chemical analysis of calcined and attrition milled powders

Component	*Chemical composition (wt%)*	
	As-calcined powder	*Calcined and attrition milled powder*
Al_2O_3	71·44 ± 0·43	66·82 ± 0·23
SiO_2	28·43 ± 0·17	26·76 ± 0·15
ZrO_2	—	6·77 ± 0·10
MgO	—	3·01 ± 0·05
$Fe_2O_3 + Na_2O + K_2O$	< 0·2	< 0·5
Al/Si molar ratio	2·96	2·94

The calcination temperature and the time of milling is given in Table 1.

balls contain $3{\cdot}31 \pm 0{\cdot}08$ wt% MgO and $0{\cdot}69 \pm 0{\cdot}01$ wt% CaO, which is in accordance to literature[13].

The representative microstructure of the uncrept specimen is shown by the SEM micrograph in Fig. 2. The morphological structure is composed of two types of grains: elongated crystals with longer axis of about 4–8 μm are embedded into a matrix of polyhedral grains with sizes of about 200–500 nm. ZrO_2-grains have equiaxed or angular shapes and are mostly dispersed intergranularly in the matrix.

HRTEM images show that a few triple points are filled with glassy phase, and very rare thin glassy films < 5 nm in diameter are observed at grain boundaries (Fig. 3). Faceted pockets that may have originally been filled with glass are also observed in rare cases. The results of EDX analyses of the glassy phase in triple point junctions, and of the adjacent mullite grains at two different areas of the sample labelled as 1 and 2, are given in Table 3. The area 1 corresponds to the HRTEM micrograph shown in Fig. 3(A). Results of EDX analysis of a glassy phase located among two mullites and a ZrO_2 grain at two different areas of the sample (1 and 2) are shown in Table 4. The area 1 corresponds to the HRTEM micrograph in Fig. 3(B). The combination of TEM imaging and linear analytical measurement of X-ray intensity distributions at uncrept specimen are shown in Figs 4–6. The intention was to prove if a glassy phase is located at the grain boundaries of adjacent mullite crystals and the mullite/ZrO_2 interfaces.

Further series of samples crept at different experimental conditions are represented by the SEM and TEM micrographs in Figs 7–9.

The mechanical characteristics of the sintered body (Vickers hardness, HV, Dynamic Young's modulus, E, fracture toughness, K_{IC}, and four-point bending strength, $\sigma_{B,4P}$) determined at room temperature are listed in Table 5. Load–displacement curves measured at different temperatures are illustrated in Fig. 10, and four-point bending strengths as a function of temperature are given in Fig. 11.

Two types of creep data were collected: (1) temperature dependence of strain rate at the applied stresses of 20 and 100 MPa, respectively, and (2) stress dependence of strain rate at two constant temperatures $T = 1200°C$ and $T = 1400°C$. A short initial stage of rapid compression is observed in all experiments before the creep rate reduces to an almost linear creep rate, as shown for data at 1400°C and stresses of 60, 80 and 100 MPa in Fig. 12.

The logarithm of the strain rates under the stress of 20 and 100 MPa versus reciprocal temperature are given in Fig. 13(A). It is obvious that one single

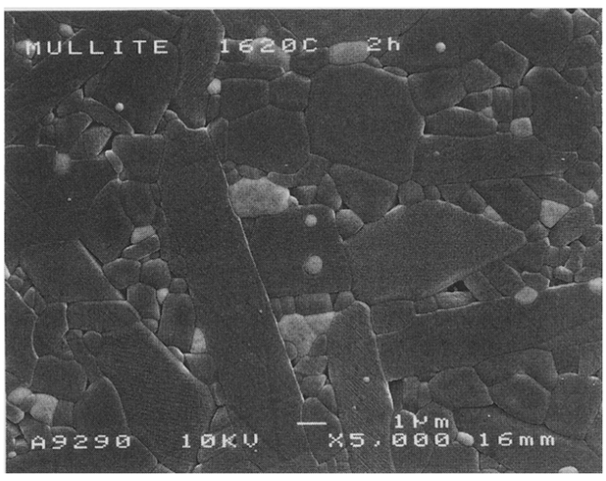

Fig. 2. A representative SEM microstructure of the studied mullite samples. Polished and thermally etched surface.

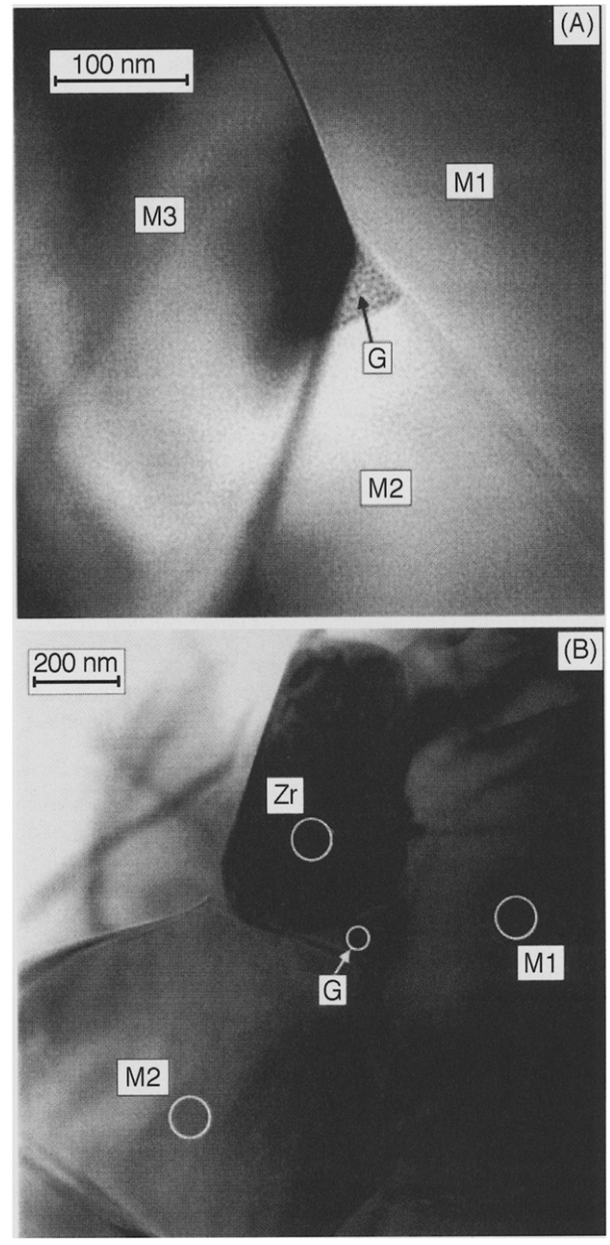

Fig. 3. HRTEM images of uncrept sample. (A) Triple junction with glassy phase among three mullite grains, (B) triple point among two mullites and a ZrO_2 grain. (G) glassy phase, M1, M2, M3-mullite and Zr-ZrO_2 grains.

Table 3. EDX analysis of glassy phase in two triple points and its adjacent mullite grains

Composition mole%	Glassy phase		*Mullite*					
	1[a]	*2*	*Area 1*			*Area 2*		
			M1[a]	*M2*[a]	M3[a]			
Al_2O_3	6·77	12·98	56·09	54·10	51·92	53·84	58·80	56·11
SiO_2	89·38	84·29	40·67	42·14	44·04	42·44	40·73	39·76
ZrO_2	1·85	1·49	0·71	1·44	1·72	1·84	0·46	1·23
MgO	1·98	1·30	2·52	2·31	2·33	1·88	—	2·89

[a]Glassy phase in the triple point (G), and the adjacent mullites (M1, M2 and M3) shown in Fig. 3(A).

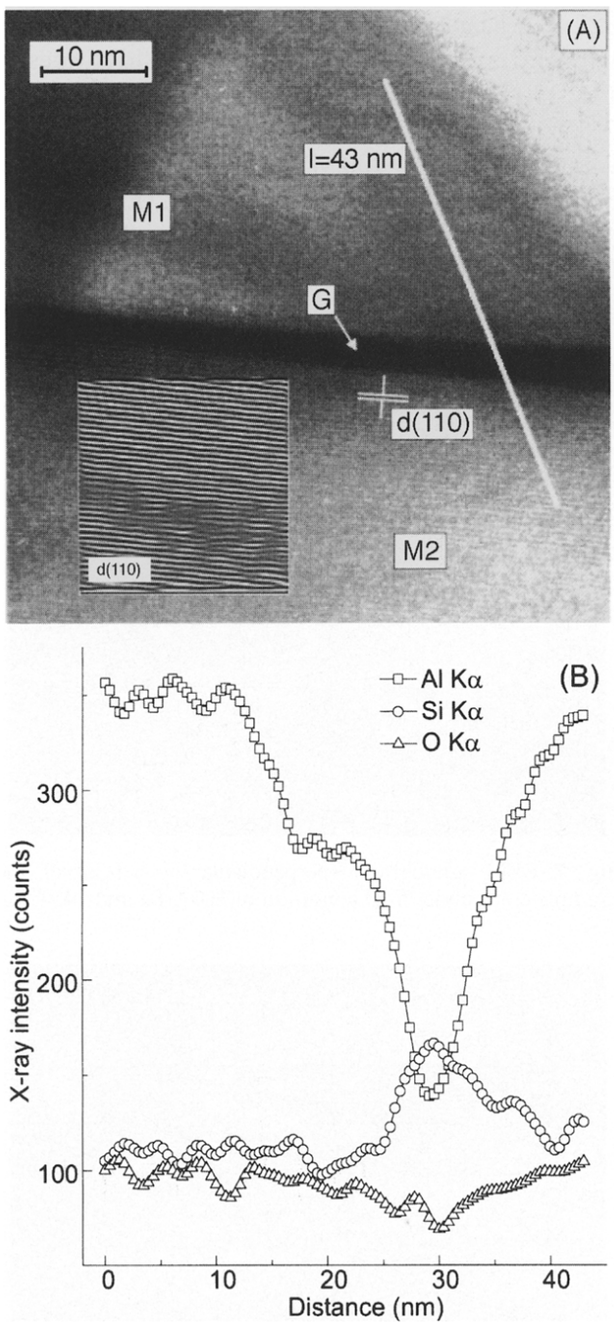

Fig. 4. (A) HRTEM image of two mullite grains (M1 and M2) and the grain boundary. Overlay: (110) lattice planes (2× magnified) of M2 gained by Fourier transformation and filtering of the original structure image. (B) EDX line analysis across the grain boundary hinting at the appearance of a glassy phase (G).

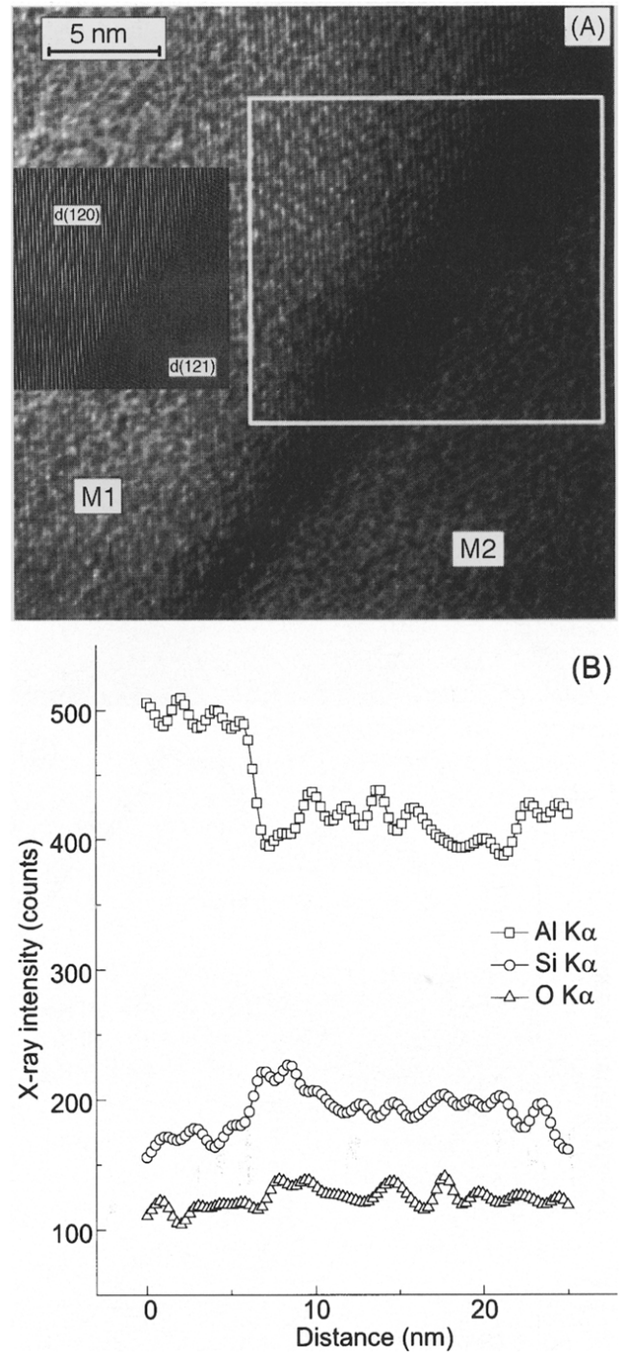

Fig. 5. (A) HRTEM image of two mullite grains. Overlay: (120) and (121) lattice planes of M1 and M2 gained by Fourier transformation and filtering of the original structure image (2× demagnified). (B) EDX-line analysis across the grain boundary.

Table 4. EDX-analysis of glassy phase in triple points among two mullites and a ZrO_2 grain

Composition mole%	*Glassy phase*		*Mullite*				ZrO_2	
	1[a]	*2*	*1*		*2*		*1*	*2*
			M1[a]	*M2*[a]			*Zr*[a]	
Al_2O_3	34·85	33·67	55·79	57·10	55·13	47·63	5·92	10·71
SiO_2	61·03	62·96	42·16	41·79	42·24	49·93	7·00	12·68
ZrO_2	1·15	1·02	0·18	0·46	0·49	0·31	86·41	76·25
MgO	2·81	2·57	1·87	1·79	2·13	2·12	0·66	0·37

[a]The micrograph of the corresponding area is shown in Fig. 3(B).

straight line for each data set does not fit well. Instead, two straight lines with significantly different slopes can be distinguished. Consequently, two different creep activation energies, Q_1, and Q_2, for each applied stress were obtained. From the slopes of the plots the activation energies $Q_1 = 363 \pm 15\,kJ\,mol^{-1}$ at the stress of $\sigma = 20\,MPa$ and $Q_1 = 321 \pm 25\,kJ\,mol^{-1}$ at the stress of $\sigma = 100\,MPa$ in temperature range of 1200 to 1300°C [dot lines in Fig. 13(A)], and the activation energies $Q_2 = 747 \pm 25\,kJ\,mol^{-1}$ at $\sigma = 20\,MPa$, and $Q_2 = 703 \pm 9\,kJ\,mol^{-1}$ at $\sigma = 100\,MPa$ in the range of 1300 and 1450°C (solid lines) are obtained. (For purpose of comparison, the data obtained by Hynes and Doremus for mullite containing small amount of glassy phase at the stress of 100 MPa[14] were also

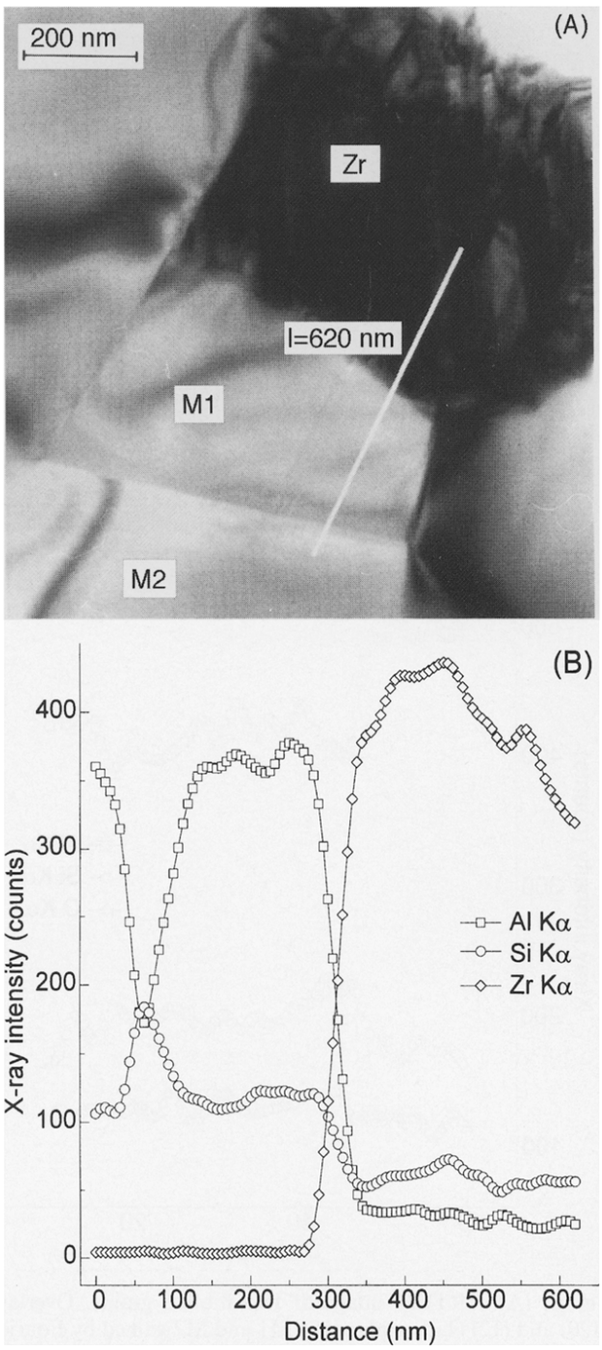

Fig. 6. (A) HRTEM image of two mullites and a ZrO_2 grain, (B) EDX-line analysis across the ZrO_2 and two mullite grains.

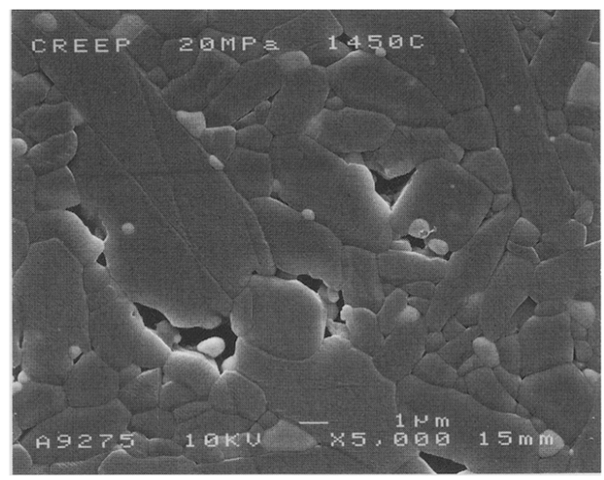

Fig. 7. SEM micrograph (perpendicular to stress) of the sample crept under final condition of 100 MPa and 1450°C.

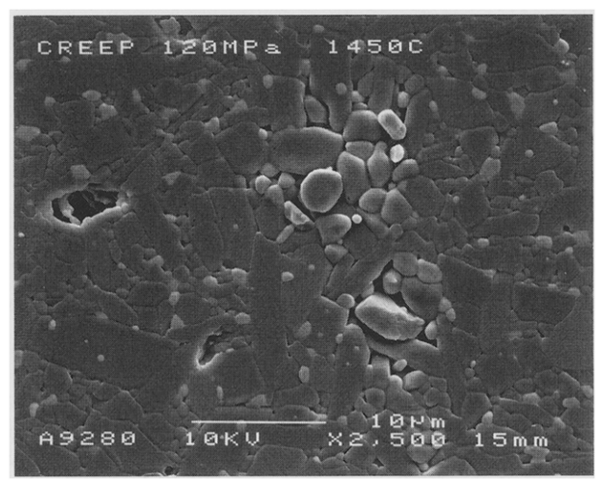

Fig. 8. SEM micrograph of the sample crept under final condition of 120 MPa and 1450°C.

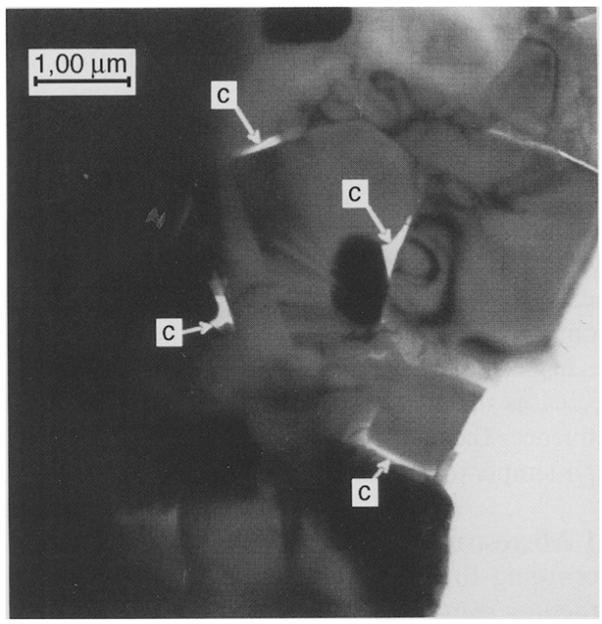

Fig. 9. HRTEM image of the same specimen as in Fig. 8: c,cavities.

Table 5. Vickers hardness, E-modulus, fracture toughness and 4-point bending strength at ambient temperature

HV (GPa)	*E-modulus (GPa)*	K_{IC} *(MPa m$^{1/2}$)*	*Bending strength (MPa)*
13·0 ± 0·4	220 ± 2	1·9 ± 0·1	237 ± 15

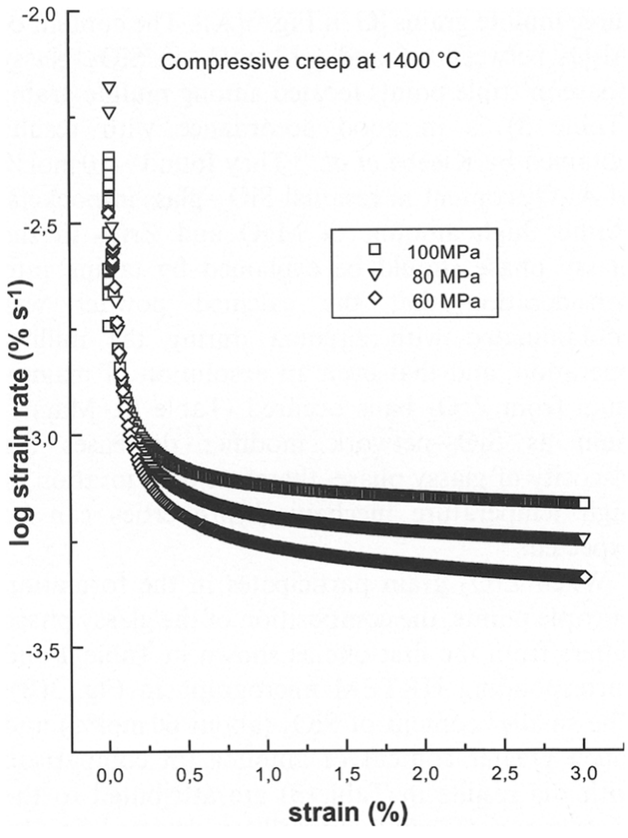

Fig. 10. Load–displacement curves at elevated temperatures. The four-point bending strength was measured at specimen ($3\times4\times45\,mm^3$) loaded at a constant feeding rate of $0{\cdot}1\,mm\,min^{-1}$, spans 20 and 40 mm.

incorporated into the figure, and the least square fit was given by dash line.) From the plot of logarithm of the true strain rate versus log of stress at $T = 1200°C$ and $T = 1400°C$, the stress exponent n equal 0·83 is obtained, as shown in Fig. 13(B).

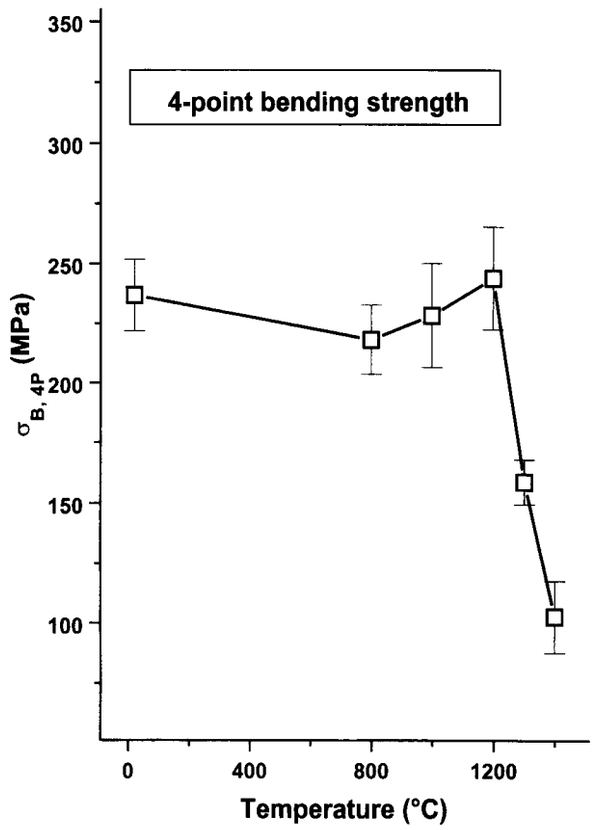

Fig. 11. Four-point bending strength as a function of temperature. The measurement conditions are given in Fig. 10.

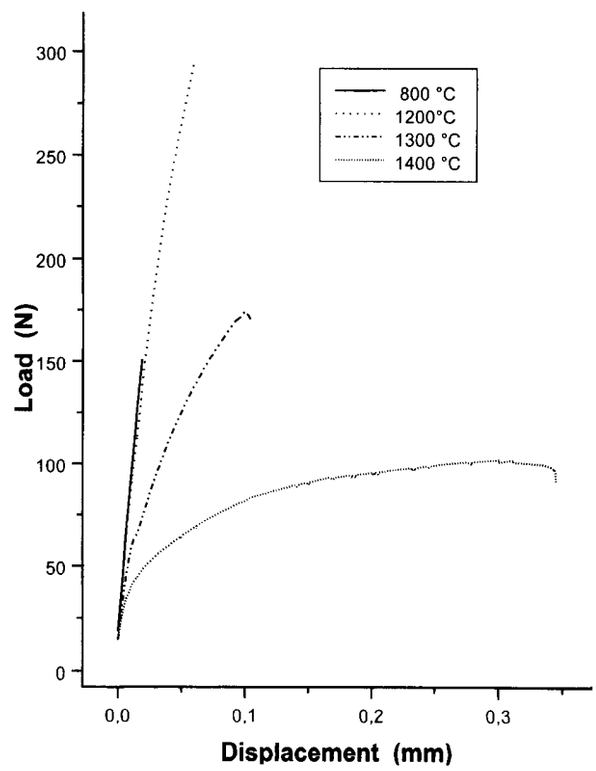

Fig. 12. Strain rates versus strain for data at 1400°C and the stresses of 60, 80 and 100 MPa.

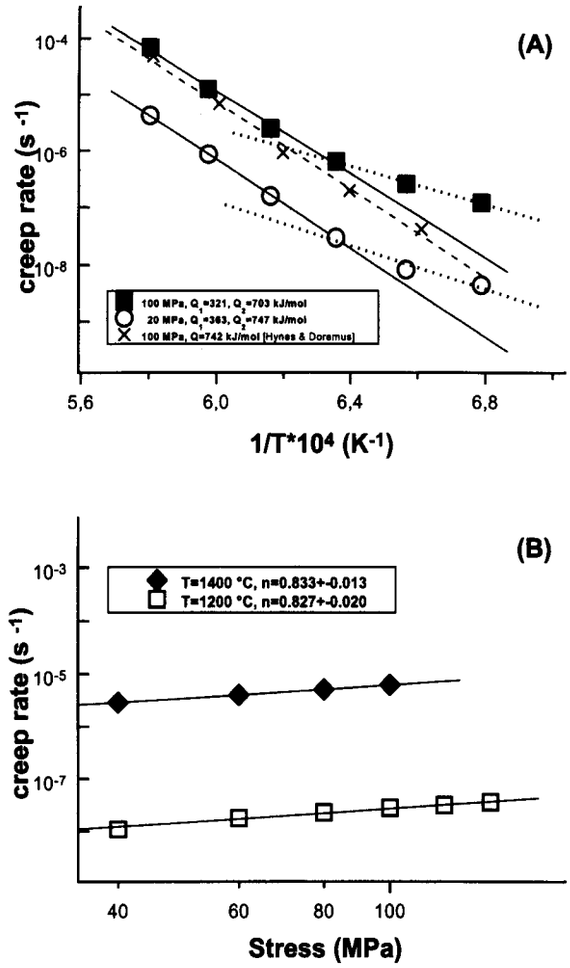

Fig. 13. (A) Strain rate as a function of reciprocal temperature at the constant stress of 20 and 100 MPa, respectively. The solid lines are least squares fits of data in the range of 1300 and 1450°C and the dot lines in the range of 1200 to 1300°C, respectively. The least square fit for data cited in literature[14] is given by dash line. The calculated activation energies [eqn (1)] are: $Q_1 = 363 \pm 15\,\text{kJ mol}^{-1}$ and $Q_2 = 747 \pm 38\,\text{kJ mol}^{-1}$ at the stress of $\sigma = 20\,\text{MPa}$, and $Q_1 = 321 \pm 25\,\text{kJ/mol}^{-1}$ and $Q_2 = 703 \pm 9\,\text{kJ mol}^{-1}$ at $\sigma = 100\,\text{MPa}$, respectively. (B) Strain rate as a function of stress at $T = 1200°\text{C}$ and $T = 1400°\text{C}$, respectively. Least square fits are given by solid lines. Calculated stress exponents [eqn (1)] are: $n = 0{\cdot}83 \pm 0{\cdot}02$ at $T = 1200°\text{C}$, and $n = 0{\cdot}83 \pm 0{\cdot}01$ at $T = 1400°\text{C}$.

4 Discussion

Al-rich mullite (64·4 mole% or 74·5 wt% of Al_2O_3, Al/Si = 3·62) is formed by calcination of the gel at 1070°C (Table 1), as was expected for single-phase gel in accordance with data in literature.[12] Since the molar ratio of Al/Si = 2·96 in the bulk sample is smaller than that in the mullite lattice, it can be supposed that the calcined powder contains a part of SiO_2 as amorphous phase. That is in agreement with the quantitative XRD analysis of calcined powder. Accordingly, it can be expected that a small amount of a liquid phase will form at about 1300°C, which enhances the sintering. Due to amorphisation of powder during milling (Fig. 1), the amount of crystalline mullite decreases from 97 to 40 wt%. Hydration of the powder takes place as well. Moreover, the powder is contaminated with 6·77 ± 0·10 wt% of zirconia and even with 3·01 ± 0·05 of MgO (Table 2). The Mg/Zr ratio is much higher than in Mg-stabilised zirconia balls, in which 3·31 ± 0·08 wt% MgO was determined. The obtained analysis of mill balls is in accordance with literature data for Mg-stabilised ZrO_2.[13] That means that a part of magnesium was leached out from ZrO_2 grains by abrasion. This fact should not be neglected, since magnesium as glass modifier decreases the viscosity of SiO_2–glassy phase which influences the microstructure and consequently the high temperature mechanical properties of mullite.

4.1 Microstructure

According to Kanka and Schneider[15] the microstructure seen in SEM micrograph (Fig. 2), i.e. elongated grains embedded into fine mullite–grain–matrix, is characteristic for liquid flow sintering. HRTEM micrographs combined with EDX analyses (Fig. 3) confirm the presence of the glassy phase in triple grain junctions, but only a small number of the junctions filled with glassy phase were found. The analyses of triple pockets located among mullite grains at two different areas are given in Table 3; the area 1 corresponds to the HRTEM micrograph in Fig. 3(A). SiO_2–rich glassy phase (> 80 mol% of SiO_2) with Al_2O_3, ZrO_2, and MgO was evaluated in triple points surrounded by three mullite grains [G in Fig. 3(A)]. The content of Al_2O_3 between ~6 and ~12 mol% in SiO_2–glassy phase in triple points located among mullite grains (Table 3) is in good accordance with results obtained by Kleebe *et al.*[16] They found ~10 mol% of Al_2O_3 content in residual SiO_2–glass in pockets. Rather high amount of MgO and ZrO_2 in the glassy phase should be explained by taking into consideration that the calcined powder was contaminated with zirconia during the milling operation, and that even an exsolution of magnesium from ZrO_2 balls occured (Table 2). Magnesium as SiO_2–network modifier decreases the viscosity of glassy phase, therefore deterioration of high temperature mechanical properties can be expected.

When ZrO_2 grain participates in the formation of triple points, the composition of the glassy phase differs from the first one as shown in Table 4 and corresponding HRTEM micrograph in Fig. 3(B). The smaller content of SiO_2 (about 60 mol%) and much greater content of alumina (in comparison with the results in Table 3) are attributed to the coexistence of small crystallites detected in the glassy phase. It can be assumed that recrystallisation of mullite occurs. However, it was impossible to assign the crystalline phase with certainty.

From Tables 3 and 4 it can be seen that Al/Si molar ratio of mullite grains varies from 2·54 to 2·70 and is smaller than in stoichiometric mullite (Al/Si = 3), due to incorporation of Zr and Mg into mullite structure. According to Schneider *et al.*[7] mullite incorporates about 0·5 wt% MgO. The incorporation of MgO is reciprocally correlated with the aluminium content of the phase. According to the same authors zirconium enters the mullite structure in small amounts too (< 0·8 wt% ZrO_2), and the amount of ZrO_2 increases with Al_2O_3 content in mullite. The values from 0·5 to 1·2 mol% ZrO_2 incorporated in mullite structure were reported by Koyama *et al.*[17] We assume that a somewhat greater incorporation of these cations in mullite structure could be attributed to simultaneous incorporation of Zr^{4+} and Mg^{2+} ions. The excess charge resulting from the incorporation of zirconium ions is compensated by magnesium. Besides, the equilibrium state of the system is not yet achieved.

Referring to the TEM image in Fig. 4, the intensity distributions of the AlK_α and SiK_α radiations [Fig. 4(B)] remarkably change in a < 5 nm thick range of the grain boundary. These fluctuations correspond to the appearance of a glassy phase. Another grain boundary region is shown by TEM structure imaging in Fig. 5. The lattice fringes of two mullite grains meet each other as shown by the processed image overlaid in the figure. The intensity course of the AlK_α line across the grain boundary [Fig. 5(B)] does not show a significant minimum as observed in Fig. 4(B), but only a steep decrease from one intensity level (corresponding to mullite with higher Al/Si ratio) to another (that corresponds to mullite with somewhat smaller Al/Si ratio). On the other hand, the corresponding intensity distribution of SiK_α shows a small maximum at grain boundary. This may not be caused by a glassy phase [as it was clearly observed in Fig. 4(B)], but by a compositional gradient in the grain boundary region.

Studying the composition and microstructure of sintered stoichiometrical mullite Mizuno[18] also found grain boundaries free from intergranular glassy film. Kleebe *et al.*[16] found wetted and nonwetted grain boundaries. It is worth to note that within ZrO_2 grains (Fig. 6), small intensities of AlK_α and SiK_α can always be observed. It can be understood as the formation of SiO_2-rich film around the ZrO_2 grains, which wets and partially dissolves the grains. This explains the EDX analysis of ZrO_2 grains given in Table 4.

4.2 Mechanical characteristics

The values of Vickers hardness, E-modulus and four-point bending strength at ambient temperature (Table 5) agree with the data in literature for dense sintered mullite[5–7]. The change of bending strength with temperature up to 1200°C (Fig. 11) is in a remarkably good agreement with the results obtained by Osendi and Baudin[5] for mullite ceramic with 0·43 wt% of total impurities. The decrease of strength above 1200°C is somewhat steeper in our measurements. It can be attributed to less viscous silica-rich glassy phase, due to higher total content of impurities, especially Mg (Tables 3 and 4) which lowers the viscosity of SiO_2–glass. Summarising the published data of high-temperature bending strengths of mullite, Schneider *et al.*[7] emphasised that depending on the mullite microstructure, two typical strength curves can be observed. The first type shows strength maxima at an elevated temperature. The second one shows no distinct maxima, but decreases slightly with the increase in temperature. The microstructure of the first type is characterised by mullite grains with small amount of glassy phase located at grain boundaries. The microstructure of the latter is characterised by mullite grains and very small amount of glassy phase, which is located only in triple points and not at grain boundaries. The temperature of maximum strength changes with chemical composition. With increasing amount of the glassy phase the maximum of the strength becomes more distinct. When alkaline and earth-alkaline cations are present, the maximum is located at lower temperatures (e.g. Na_2O forms liquid even at 1000°C, consequently it detrimentally effects the high-temperature mechanical properties). As seen in Fig. 11, the maximum strength of mullite at 1200°C (244 ± 21 MPa) is only slightly higher than the strength at 800°C (218 ± 14 MPa), what can be related to a low viscous magnesium containing liquid. Mg incorporation into the glassy phase was confirmed by EDX analysis (Tables 3 and 4).

A small plastic deformation is observed prior to the failure in the load displacement curve at 1200°C (Fig. 10), whereas a considerable plastic deformation prior to the failure at 1400°C occurs. According to Ohira *et al.*[6] if a glassy phase exists at grain boundaries, the fracture at elevated temperatures is preceded by a plastic deformation.

Temperature dependence of the creep rates at 20 and 100 MPa is shown in Fig. 13(A). Two straight lines on creep rates data with significantly different slopes can be distinguished, not depending on whether the measurement was carried out under the stress of 20 or 100 MPa. The creep rates under the stress of 20 MPa were only an order of magnitude smaller. The activation energies obtained in temperature range 1200–1300°C were 321 ± 25 kJ mol^{-1}

(100 MPa) and $363 \pm 15\,kJ\,mol^{-1}$ (20 MPa). In the temperature range 1300–1450°C the values of $747 \pm 38\,kJ\,mol$ and $703 \pm 9\,kJ\,mol$, respectively, were obtained. Studying the creep behaviour of mullite containing small amount of glassy phase, Nixon *et al.*[19] observed even three branches in the creep rate data in the temperature range 1177–1427°C, and constant stress exponent $n \sim 1$ in the whole temperature range. The activation energies of the first and the third branch ($357 \pm 44\,kJ\,mol^{-1}$ and $754 \pm 19\,kJ\,mol^{-1}$, respectively) match well with our results [Fig. 13(A)]. Hynes and Doremus[14] evaluated the activation energy of $742\,kJ\,mol^{-1}$, and $n = 1{\cdot}6$ for mullite with glassy phase in the range of 1230–1447°C (at the same stress of 100 MPa). For reason of comparison their data are given in Fig. 13(A). Ashizuka *et al.*[20] found, that if the creep rate is controlled by grain boundary sliding due to the intergranular glassy phase, only a small change in the creep behaviour occurs by adding of ZrO_2. Accordingly, the two branches seen by us cannot be attributed to ZrO_2, but to the property of the mullite. We also found a somewhat smaller value of stress exponent $n = 0{\cdot}83$ [Fig. 13(B)] in comparison to data obtained by Nixon *et al.*[19] According to Ashizuka *et al.*[20] it can be attributed to the presence of ZrO_2 in the system. The obtained data clearly show that rate controlling mechanism below 1300°C differs from that above. Below 1300°C, it is most likely controlled by grain boundary sliding accommodated by solution-precipitation in the glassy phase, and above by grain boundary sliding by viscous flow of SiO_2-rich glassy phase. Due to the low viscous glassy phase (caused by the greater amount of glass modifiers) the specimen crept an order of magnitude faster than pure mullite cited in literature. SEM micrographs of crept specimen under conditions of 20 MPa and 1450°C revealed the formation of intergranular crack propagation located at interfaces along elongated grains (Fig. 7). The average sizes of elongated as well as submicron grains did not change significantly during the creep tests as seen by comparison SEM micrographs of uncrept and crept specimen (Figs 2 and 7). Contrary to Nixon's observation that cavities formed during the creep experiments at ~1290°C are filled with glassy phase at higher temperatures,[19] the most cavities in the investigated crept specimen remained empty even at 1450°C and 100 MPa. It is also a confirmation that only a small amount of glassy phase is formed during sintering. Under more severely experimental conditions (stress 120 MPa) 'creep damage zones' about 15 μm in size were formed (Fig. 8). The empty cavities at the grain boundaries are also observed in HRTEM micrograph in Fig. 9.

5 Conclusion

1. The wearing out of ZrO_2 used as milling media by disintegration of mullite powder is rather high; 6·77 wt% ZrO_2 and even 3·01 wt% MgO was determined in the milled powder. ZrO_2 particles are mostly intergranularly incorporated in microstructure of sintered bodies. Magnesium as SiO_2–network modifier enters the glassy phase. HRTEM images and EDX analyses confirmed magnesium in the residual glassy phase in triple points. The steep decrease of bending strength above 1200°C and an order of magnitude higher creep rates than it is described for mullite (without glassy phase) are attributed to the low viscous magnesium containing liquid.
2. Microstructure of prepared mullite ceramics is characterised by bimodal particle size distribution. Elongated grains 4–8 μm are embedded in matrix with smaller equidistant particles. That is characteristic of liquid flow sintering of mullite.
3. Grain boundary glassy films < 5 nm thick were rare observed by HRTEM images and EDX line analyses.
4. The microstructural observations of glassy film, activation energies, stress exponent and magnitude of the creep rates suggest that the creep is controlled by the solution-precipitation mechanism accommodating grain–boundary sliding below 1300°C, and by the grain boundary sliding by viscous flow of SiO_2–rich glassy phase above that temperature.

References

1. Somiya, S. and Hirata, Y., Mullite powder technology and applications in Japan. *Am. Ceram. Soc. Bull.*, 1991, **70**, 1624–1632.
2. Baudín, C., Miranzo P. and Osendi, M. I., High temperature mechanical behaviour of $3Al_2O_3{\cdot}2SiO_2$ mullite based ceramics. In *Third Euro-Ceramics V-3*, Faenza, Editrice Iberica S.L. Spain, 1993, pp. 369-375.
3. Vogel, W., *Glas Chemie*. Springer–Verlag, Berlin, Heidelberg, 1992.
4. Dokko, P. C., Pask, J. A. and Mazdiyasni, K. S., High temperature mechanical properties of mullite under compression. *J. Am. Ceram. Soc.*, 1977, **60**, 150–155.
5. Osendi, M. 1. and Baudín, C., Mechanical properties of mullite materials. *Journal of the European Ceramic Society*, 1996, **16**, 217–224.
6. Ohira, H., Ismail, M. G. M. U., Yamamoto, Y., Akiba, T. and Sômiya, S., Mechanical properties of high purity mullite at elevated temperatures. *Journal of the European Ceramic Society*, 1996, **16**, 225–229.
7. Schneider, H., Okada, K. and Pask, J., *Mullite and Mullite Ceramics*. John Wiley and Sons, Chichester, U.K., 1994.
8. Nass, R., Tkalcec, E. and Ivankovic, H., Single-phase gels doped with chromium. *J. Am. Ceram. Soc.*, 1995, **78**, 3097–3106.

9. Cameron, W. E., Composition and cell dimensions of mullite. *Am. Ceram Soc. Bull.*, 1997, **56**(11), 1003–1011.
10. Anstis, G. R., Chanticul, P., Lawn, B. R. and Marshall, D. B., A critical evaluation of indentation techniques for measuring fracture toughness: I, Direct crack measurements. *J. Am. Ceram. Soc.*, 1981, **64**, 533–538.
11. Itatani, K., Kubozono, T., Howell, F. S., Kishioka, A. and Kinoshita, M., Some properties of mullite powders prepared by chemical vapour deposition. Part 1. Preparation of mullite powder. *J. Mat. Sci.*, 1995, **30**, 1158–1165.
12. Okada K. and Ôtsuka, N., Formation process of mullite. In *Mullite and Mullite Matrix Composites, Ceramic Transactions*, Vol. 6, ed. S. Somiya, R. F. Davis and J. A. Pask. American Ceramic Society, Westerville, OH, 1990, pp. 375-387.
13. Porter, D. L. and Heuer, A. H., Microstructural development in MgO–partially stabilized zirconia (Mg–PSZ). *J. Am. Ceram. Soc.*, 1979, **62**, 298–305.
14. Hynes, A. P. and Doremus, R. H., High-temperature compressive creep of polycrystalline mullite. *J. Am. Ceram. Soc.*, 1991, **74**, 2469–2475.
15. Kanka, B. and Schneider, H., Sintering mechanisms and microstructural development of coprecipitated mullite. *J. Mat. Sci.*, 1994, **29**, 1239–1249.
16. Kleebe, H. J., Hilz, G. and Ziegler, G., Transmission electron microscopy and electron energy-loss spectroscopy characterization of glass phase in sol–gel–derived mullite. *J. Am. Ceram. Soc.*, 1996, **79**(10), 2592–2600.
17. Koyama, T., Hayashi, S., Yasumori, A., Okada, K., Schmucker, M. and Schneider, H., Microstructure and mechanical properties of mullite/zirconia composites prepared from alumina and zircon under various firing conditions. *Journal of the European Ceramic Society*, 1996, **16**, 231–237.
18. Mizuno, M., Microstructure, microchemistry, and flexural strength of mullite ceramics. *J. Am. Ceram. Soc.*, 1991, **74**, 3017–3022.
19. Nixon, R. D., Chevacharoenkul, S., Davis, R. F. and Tiegs, T. N., Creep of hot-pressed SiC whisker reinforced mullite. In *Mullite and Mullite Matrix Composites*, Ceramic Transactions, Vol. 6, ed. S. Somiya, R. F. Davis and J. A. Pask. American Ceramic Society, Westerville, OH, 1990, pp. 311-322.
20. Ashizuka, M., Honda, T. and Kubota, Y., Creep in mullite ceramics containing zirconia. *J. Ceram. Soc. Jpn.*, 1991, **99**, 357–360.